

ESCAPING PARTICLE FLUXES IN THE ATMOSPHERES OF CLOSE-IN EXOPLANETS. II. REDUCED MASS LOSS RATES AND ANISOTROPIC WINDS

J. H. Guo¹

National Astronomical Observatories/Yunnan Observatory, Chinese Academy of Sciences,
P.O. Box 110, Kunming 650011, China; guojh@ynao.ac.cn

Received _____; accepted _____

¹Key Laboratory for the Structure and Evolution of Celestial Objects, CAS, Kunming
650011, China

ABSTRACT

In Paper I, we presented a one-dimensional hydrodynamic model for the winds of close-in exoplanets. However, close-in exoplanets are tidally locked and irradiated only on the day sides by their host stars. This requires two-dimensional hydrodynamic models with self-consistent radiative transfer calculations. In this paper, for the tidal locking (two-dimensional radiative transfer) and non-tidal locking cases (one-dimensional radiative transfer), we constructed a multi-fluid two-dimensional hydrodynamic model with detailed radiative transfer to depict the escape of particles. We found that the tidal forces (the sum of tidal gravity of the star and centrifugal force due to the planetary rotation) supply significant accelerations and result in anisotropic winds. An important effect of the tidal forces is that it severely depresses the outflow of particles near the polar regions where the density and the radial velocity are a factor of few-ten smaller than those of the low-latitude regions. As a consequence, most particles escape the surface of the planet from the regions of low-latitude. Comparing the tidal and non-tidal locking cases, we found that their optical depths are very different so that the flows also emerge with a different pattern. In the case of the non-tidal locking, the radial velocities at the base of the wind are higher than the meridional velocities. However, in the case of tidal locking, the meridional velocities dominate the flow at the base of the wind, and they can transfer effectively mass and energy from the day sides to the night sides. Further, we also found that the differences of the winds show middle extent at large radii. It expresses that the structure of the wind at the base can be changed by the two-dimensional radiative transfer due to large optical depths, but the extent is reduced with an increase in radius. Because the escape is depressed in the polar regions, the mass loss rate predicted by the non-tidal locking model, in the order of magnitude of 10^{10} g

s^{-1} , is a factor of 2 lower than that predicted by one-dimensional hydrodynamic model. The results of tidal locking show that the mass loss rate is decreased a order of magnitude, only $4.3 \times 10^9 \text{ g s}^{-1}$, due to large optical depths on the night side. We also found that the distributions of hydrogen atoms show clear variations from the day side to night side, thus the origin of the excess absorption in Ly α should be reexamined by using multi-dimensional hydrodynamic models.

Subject headings: hydrodynamics - planetary systems - planets and satellites:
atmospheres - planets and satellites: individual (HD 209458b)

1. INTRODUCTION

The excess absorption in Lyman α of HD 209458b and HD 189733b have been found by Vidal-Madjar et al. (2003) and Lecavelier des Etangs et al. (2010). From the excess absorption those authors suggested that the hydrogen clouds of HD 209458b and HD 189733b are above their Roche lobe. Most of the explanations attribute the excess absorption to mass loss from the surfaces of exoplanets (Lammer et al. 2003; Lecavelier des Etangs et al. 2004; Yelle 2004, 2006; Tian et al. 2005; García Muñoz 2007; Penz et al. 2008; Murray-clay et al. 2009; Lammer et al. 2009; Guo 2011 (Paper I)). To simplify the calculations, all the hydrodynamic models above are one dimensional. Recently, two- and three-dimensional hydrodynamic models have been presented by Stone & Proga (2009) and Schneider et al. (2007), however, some challenging physical processes have been neglected by them. All the above one-dimensional models described thermal particle escape, namely, the particles of the planets escape from their gravity potential wells as a result of the irradiation from the host star. However, the charge exchange between the stellar wind and the planetary escaping exosphere can result in the same observation phenomenons (Holmström et al. 2008). The loss of nonthermal neutral atoms via interactions between the stellar wind and the exosphere have been discussed by many researchers (Erkaev et al. 2005; Holmström et al. 2008; Ekenbäck et al. 2010). Their results showed that the fresh neutral atoms produced by the charge exchange can match the Ly α excess absorption.

Although current theoretic models predicted the mass loss at the upper atmosphere of Hot Jupiters, no clear observational evidences support the thermal or non-thermal explanations. Either the energetic HI of stellar origin or thermal HI populations in the planetary atmosphere can fit the observations of Ly α (Ben-Jaffel & Hosseini 2010). Moreover, Koskinen et al. (2010) found that the excess absorption can be explained solely by absorption in the upper atmosphere and the process of charge exchange might not be

necessary. According to the examples from our solar system, however, the charge exchange can play an important role in explaining the excess Ly α absorption (see Lammer 2011 for more details).

The extent of understanding the excess absorption depends strongly on the physics described in theoretical models. To fully distinguish the thermal or non-thermal processes, the single-fluid and one-dimensional models are not enough. Yelle (2004) and García Muñoz (2007) have used the diffusion approximation to depict the velocity differences between different species, and photochemistry, ionization and recombination have also been included. Moreover, Guo (2011) presented a multi-fluid one-dimensional model to depict the atmospheric escape and predicted reasonable mass loss rates for HD 209458b and HD 189733b. The multi-fluid model is more advantageous than single-fluid one because the interactions among different species between the stellar and planetary winds are depicted by its own continuity, momentum and energy equations. However, the model of Paper I can be improved in two points at least. First, the one-dimensional hydrodynamic model only simulates the case along the line connecting the center of planet and the center of the star. For the close-in exoplanets, the tidal forces between the star and planet tend to circularize the orbit and synchronize the rotation of the planet with the orbital period (Guillot et al. 1996; Trilling 2000). Thus, for the close-in exoplanets it is reasonable to assume that their same sides are always facing the star. If the irradiation and tidal effects of the host star are included, multi-dimensional models are more suitable. Second, the constraint of stellar wind has been omitted. Stone & Proga (2009) discussed the interaction between the stellar and planetary winds and found that the planetary wind is confined to a small volume by the stellar wind. However, their model used the assumption of a single-fluid so the processes of charge exchange could not be simulated.

These issues as above motivated us to construct a two-dimensional hydrodynamic

model with realistic treatment of radiative transfer and tidal forces. We have developed a time-independent model with the one-dimensional assumption, however, it is impractical to extend the method to two-dimension because of the existence of critical points. In this paper we constructed a time-dependent two-dimensional model including the micro-physics processes, the influence of tide and radiative transfer. The interactions between the stellar and planetary winds will be discussed in the further work.

This paper aims to calculate the escape of atomic hydrogen and protons through the solution to their mass, momentum and energy equations. The microscopic physics processes are covered in the mass, but not in the momentum and energy equations (Section 2.1). The processes of radiative transfer are discussed in Section 2.2. We used semi-implicit scheme to calculate these equations (Section 2.3) and tested the model in Section 3. We incorporated one- and two-dimensional radiative transfer into the hydrodynamic models (Section 4), and focus on the differences between them. In Section 5 we discussed the influence of the boundary conditions and stellar activity. Our results are summarized in Section.6

2. THE MODEL

2.1. Equations and Assumptions

In Paper I (Guo 2011) we described a steady-state, radial expansion of plasma containing three species: atomic hydrogen (h), protons (p) and electrons (e). In this paper, we extend the previous work to two-dimensions. But thermal electrons are not included. Atomic hydrogen (h) and protons (p) have their own continuity equations and are described by a particle density n_h and n_p . Since this model deals with a mixture of atomic hydrogen and protons, the following processes are considered: photoionization and recombination. Further, we assumed that the velocities and temperatures of the particles are the same,

namely, $u_h = u_p = u$ and $T_h = T_p = T$. The assumption is acceptable because the mass loss rates predicted by this model are higher than 10^9 g s^{-1} (see Section 3 and 4), if the mass loss rates are below the value the velocities and temperature should be calculated separately because of the decoupling of particles (Guo 2011). As in Paper I, we did not include H_2 in this model because the thermosphere of close-in planets should be composed primarily of H and H^+ . The location of transition from H_2 to H is about $1.1R_p$ (Yelle 2004).

We described the planetary wind by using multi-particle two-dimensional hydrodynamic equations that can be written as

$$\frac{\partial n_j}{\partial t} + \nabla \cdot (n_j \mathbf{u}) = S_j \quad (1)$$

$$\frac{\partial (n\mathbf{u})}{\partial t} + \nabla \cdot (n\mathbf{u}\mathbf{u}) + \nabla p = n\mathbf{a}_{ext} \quad (2)$$

$$\frac{\partial [n(e + \frac{u^2}{2})]}{\partial t} + \nabla \cdot [n\mathbf{u}(e + \frac{u^2}{2})] + \nabla(p\mathbf{u}) = n\mathbf{a}_{ext} \cdot \mathbf{u} + Q, \quad (3)$$

where $n_j(j=h,p)$ is particle number density of hydrogen atoms and ions. $n=n_h+n_p$ is the number density of the gas as a whole. S_j denotes the production/destruction of particles. The specific internal energy is $e = \frac{\mathcal{R}T}{\gamma-1}$, and $u^2 = u_r^2 + u_\theta^2$ is the sum of squares of velocities, where \hat{r} and $\hat{\theta}$ velocities are u_r and u_θ . γ is set to 5/3. The accelerations produced by the gravities of planet and star as well as the centrifugal forces due to the rotation of the planet around the star are included in the term of \mathbf{a}_{ext} . The net heating rate is expressed as $Q = H - L$, where H is the heating from irradiation of the star and L is cooling due to the atmospheric radiation.

The hydrodynamic equations are solved in spherical polar (r,θ) coordinates. Here $\theta=0$ is the direction towards the star, and $\theta=\pi$ is the direction away from the star. In

conservation form, these equations can be expressed as

$$\frac{\partial Q}{\partial t} + \frac{\partial F}{\partial r} + \frac{\partial G}{\partial \theta} = S_1 + S_2, \quad (4)$$

where Q is the state vector, F and G are the flux vectors, S_1 denotes the contributions from the planetary gravity and the tidal forces of stars, and S_2 includes the source/sink terms that are relative with photoionization/recombination and heating/cooling.

The state vector Q are defined as

$$Q = \begin{bmatrix} Q_1 \\ Q_2 \\ Q_3 \\ Q_4 \\ Q_5 \end{bmatrix} = \begin{bmatrix} n_h r^2 \sin \theta \\ n_p r^2 \sin \theta \\ (n_h + n_p) r^2 \sin \theta u_r \\ (n_h + n_p) r^2 \sin \theta u_\theta \\ (n_h + n_p) r^2 \sin \theta (e + \frac{u^2}{2}). \end{bmatrix} \quad (5)$$

The flux vector $[F, G]$ and the source terms S_1 are defined as

$$F = \begin{bmatrix} \frac{Q_1 Q_3}{Q_1 + Q_2} \\ \frac{Q_2 Q_3}{Q_1 + Q_2} \\ \frac{Q_3^2}{Q_1 + Q_2} + a^2 (Q_1 + Q_2) \\ \frac{Q_3 Q_4}{Q_1 + Q_2} \\ \frac{Q_3 Q_5}{Q_1 + Q_2} + a^2 Q_3 \end{bmatrix} \quad (6)$$

$$G = \begin{bmatrix} \frac{Q_1 Q_4}{r(Q_1 + Q_2)} \\ \frac{Q_2 Q_4}{r(Q_1 + Q_2)} \\ \frac{Q_3 Q_4}{r(Q_1 + Q_2)} \\ \frac{Q_4^2}{r(Q_1 + Q_2)} + \frac{a^2 (Q_1 + Q_2)}{r} \\ \frac{Q_4 Q_5}{r(Q_1 + Q_2)} + \frac{a^2 Q_4}{r} \end{bmatrix} \quad (7)$$

$$S_1 = \begin{bmatrix} 0 \\ 0 \\ 2a^2 \frac{(Q_1+Q_2)}{r} + \frac{Q_4^2}{r(Q_1+Q_2)} + (Q_1 + Q_2)a_r \\ a^2 \frac{(Q_1+Q_2) \cos \theta}{r \sin \theta} - \frac{Q_3 Q_4}{r(Q_1+Q_2)} + (Q_1 + Q_2)a_\theta \\ Q_3 a_r + Q_4 a_\theta \end{bmatrix}, \quad (8)$$

where $a = \sqrt{\mathcal{RT}}$ is the isothermal sound velocity, and a_r and a_θ are the accelerations in \hat{r} and $\hat{\theta}$ directions, respectively. The accelerations are given by

$$a_r = -\frac{\partial U}{\partial r}, \quad (9)$$

$$a_\theta = -\frac{1}{r} \frac{\partial U}{\partial \theta}. \quad (10)$$

For the position vector $\mathbf{x} = (r, \theta)$, the effective potential U is given by

$$U(\mathbf{x}) = -\frac{GM_p}{|\mathbf{x}|} - \frac{GM_p}{|\mathbf{x} - D|} - \frac{1}{2} |\Omega \times \mathbf{x}|^2, \quad (11)$$

where D is the distance of star, $\Omega = [G(M_* + M_p)/D^3]^{1/2}$ is the angular velocity of orbital plane, and M_* and M_p are the stellar and planetary mass, respectively. Finally, we can obtain the accelerations as

$$a_r = -\frac{GM_p}{r^2} + \frac{GM_*(D \cos \theta - r)}{(D^2 + r^2 - 2Dr \cos \theta)^{3/2}} - G \frac{M_*}{D^3} \cos \theta (D - r \cos \theta) \quad (12)$$

$$a_\theta = -\frac{GM_* D \sin \theta}{(D^2 + r^2 - 2Dr \cos \theta)^{3/2}} + G \frac{M_*}{D^3} \sin \theta (D - r \cos \theta). \quad (13)$$

In Equation (12), the first term represents the gravity of planet. The second and third terms as well as the two terms of Equation (13) are the accelerations produced by the

gravity of host stars and orbital motion, respectively. Except the first term of Equation (12), we refer to the other terms as "tidal accelerations". How do the tidal accelerations alter the behaviors of flows? We can estimate this by considering some special cases. In the case of $\theta = 0^\circ$, Equation (12) can be simplified to $a_r = -\frac{GM_p}{r^2} + \frac{GM_*}{(D-r)^2} - G\frac{M_*}{D^3}(D-r)$. This form is consistent with the Equation (15) of García Muñoz (2007) and hints that the tidal forces supply positive acceleration along the line connecting the planet to the star. However, the radial tidal acceleration gradually decreases with the increase of θ and become negative at $60^\circ \lesssim \theta \lesssim 120^\circ$. This means that the escape of particles in the polar regions can be depressed by the tidal forces. In addition, we also note that \hat{a}_θ is always negative (positive) if the θ is smaller (greater) than $\sim 90^\circ$. These characteristics will also be discussed further in Section 4.

The Coriolis forces have been neglected in the calculations. In the regions close to host stars, the escape velocities of particles which are in the order of magnitude of 20-40 km s⁻¹ are smaller than the orbital velocities (in the order of magnitude of 100 km s⁻¹). This means that the planetary wind can be deflected by Coriolis forces. However, our calculations are limited to the regions close to exoplanets where the velocity of the wind is much less than the orbital velocity. Thus, Coriolis forces can be neglected safely near the planet.

The source terms S_2 can be expressed as

$$S_2 = \begin{bmatrix} \frac{Q_2^2}{r^2 \sin \theta} \gamma_{rec} - Q_1 \gamma_{pho} \\ Q_1 \gamma_{pho} - \frac{Q_2^2}{r^2 \sin \theta} \gamma_{rec} \\ 0 \\ 0 \\ r^2 \sin \theta (H - L) / m_H \end{bmatrix}, \quad (14)$$

where m_H is the mass of hydrogen atom, $\gamma_{pho} = \sum_\nu \frac{F_\nu e^{-\tau_\nu}}{h\nu} \sigma_\nu$ s⁻¹ (where F_ν is photon energy

at frequency ν , τ_ν is the optical depth at frequency ν , the cross section of photoionization of hydrogen is $\sigma_\nu = 6 \times 10^{-18} (h\nu/13.6\text{eV})^{-3} \text{ cm}^2$ (Murray-Clay et al. 2009)) and $\gamma_{\text{rec}} = 2.7 \times 10^{-13} (\frac{T}{10^4})^{-0.9} \text{ cm}^{-3}\text{s}^{-1}$ (Murray-Clay et al. 2009) represent the photoionization and recombination rates, respectively. In the continuity equation, the sources and sinks to the particle flux density are due to photoionization and recombination. In energy equation, the sources and sinks are heating and cooling, respectively.

The heating processes in the mixed flows are complex. The models of Murray-Clay et al. (2009) and Paper I in which the heating from the host stars is simplified to a single photon of 20 eV predicted reasonable mass loss rates. However, the assumption of single photon energy could miss some important physical processes, such as the penetration of higher energy photons deeper in the atmosphere. In fact, the stellar radiation ionizes the species to produce high-energy photoelectrons that share their energy with other species via collisions. The heating of exoplanet atmospheres mainly comes from photoelectrons produced by photoionization, therefore, here we included EUV irradiance shortward of 912 Å, namely, the threshold value of photoionization in hydrogen atoms.

In an ionized atmosphere composed of H and H⁺, photoelectrons distribute their energy via the collision with thermal electrons. H⁺ obtain energy from thermal electrons via Coulomb collisions while hydrogen atoms share the energy of thermal electrons by elastic and inelastic collisions. Here we assumed that H and H⁺ have the same temperatures, therefore, the total heating of the atmosphere can be written as

$$H = n_h \sum_{\nu} \eta_{\nu} F_{\nu} e^{-\tau_{\nu}} \sigma_{\nu}. \quad (15)$$

For different photon energies, we defined the net heating efficiency as $\eta_{\nu} = (h\nu - 13.6)/h\nu$ that is the maximum heating efficiency. In fact, the fraction of photon energy deposited as heat in the atmosphere of exoplanet should be smaller than the definition above. It also shows that the heating efficiency is higher for the photons with higher energy. Equation

(15) hints that the contributions of heating by lower energy photons are comparable with those of higher energy photons because the heating of atmosphere is proportional to heating efficiency, but is inversely with cube of cross section of photoionization.

The cooling rate adopted in the models of Murray-Clay et al. (2009) and Paper I assumed that the atmosphere is optically thin in the Ly α line. Murray-Clay et al. (2009) have also validated that a photon can diffuse out of the wind in a typical mass loss rate of 10^{10} g s $^{-1}$ (see Appendix C of Murray-Clay et al. 2009). However, the observations indicate that the atmosphere is optically thick even in the wings of Ly α . Therefore, it is uncertain if the Ly α cooling should be included. Here we included the radiative cooling by recombination and free-free radiation, namely,

$$L = L_{rec} + L_{ff} \text{ergcm}^{-3}\text{s}^{-1}. \quad (16)$$

In addition, we can not calculate the infrared emission of H $_3^+$ as done by Yelle (2004) and García Muñoz (2007) due to the lack of photochemistry in our model. The cooling of H $_3^+$ could be important because it can modify the location of maximum temperature, but the mass loss rates are not affected by the cooling of H $_3^+$ (Penz et al. 2008).

There are not resolved emission spectra from the host stars of exoplanets. For HD 209458, we used the EUV spectra of the sun as its emission spectra. Those data are taken from Richards et al. (1994). Our calculations are completed with a solar proxy $P_{10.7} = 80$ that corresponds to a middle-low level of stellar activity.

2.2. Radiative transfer

The radiative transfers are the most important processes in determining the atmospheric structure of planet. In the case of non-tidal locking, both hemispheres of the planet can

receive the irradiation from its host star. Thus, the one-dimensional radiative transfer can approximately depict the process. In the assumption of 1D radiative transfer, the optical depth at frequency ν can be written as

$$\tau_\nu = \int_{R_{max}}^r n_h \sigma_\nu dr. \quad (17)$$

Clearly, Equation (17) shows that the optical depth is function of radii, but is not relative with θ . Thus, it cannot correctly depict the penetration of the EUV radiation from the face of day-side to night-side if the planets are tidally locked by their host stars. To calculate an accurate optical depth in the case of tidal locking, two-dimensional radiative transfer calculations are needed. Here we present a simplified treatment in which both the impact factor $q(r, \theta) = r \sin \theta$ and latitude θ determine the final optical depths. For each grid point, the nodal points at every radii are found along the opposite direction of stellar radiation, and the values of latitude at those radii are determined (see Figure 1). For a given grid point P(i, j), the nodal point at the next radius r_{i+1} can be expressed as P(i+1, j') (Note that the impact factor $q(r, \theta)$ of the given grid point P(i, j) is same with that of P(i+1, j')). Generally, the latitude of P(i+1, j') is between grid points θ_j and θ_{j-1} rather than consistent with the grid points of angular direction. Finally, the corresponding number density of P(i+1, j') at radius r_{i+1} can be approximated as $\overline{n_h} = \frac{n_{i+1,j} + n_{i+1,j-1}}{2}$. Therefore, the optical depth along the z-direction (the direction of stellar radiation) can be approximated to

$$\tau_\nu^{i,j} = \int_{z_{max}}^p \overline{n_h} \sigma_\nu dz. \quad (18)$$

The optical depth is set to 10^{10} when the impact factor q is smaller than R_p . Equation (18) is used to calculate the radiative transfer of tidal locking.

The simplified calculations represent the variations of the optical depth at all grid

points. We believe that small differences due to the approximation do not affect the results quantitatively.

2.3. Numerical Method and Boundary Conditions

The two-dimensional time-dependent multi-fluid model is integrated in time by using the fourth-stage Runge-Kutta method. For the space derivative, central difference scheme is used. To solve Equation (4), we must handle those source terms in the continuity and energy equations because of their stiffness. An explicit method could result in a long time-marching and incorrect results. Thus, we choice a semi-implicit method to deal with S_2 of Equation (4).

Equation (4) is discretized on a grid of 221 radial and 121 angular cells. We selected exponentially spaced grid in radii,

$$r_i = qr_{i-1}, q = \exp\left(\frac{\ln \frac{r_{IMAX}}{r_1}}{IMAX - 1}\right) \quad (19)$$

where i is a number of a given grid point, IMAX is the maximum number of grid points, and r_1 and r_{IMAX} denote the first and last grid points. The grid size increases exponentially with the increase of radius. We used a uniform grid in $\hat{\theta}$ direction.

The lower boundary conditions at $r = R_p$ are fixed (R_p is the planetary radius). The effective temperatures of hot Jupiter estimated by Burrows et al. (2001) are in the range of 1000 - 1500K, which is consistent with the IR thermal emission measurements (Deming et al. 2005; Charbonneau et al. 2005; Deming et al. 2006). Thus, we set $T = 1500\text{K}$ at the bottom of the flow. Here the pressure at the base of the wind is maintained on the level of $P_{R_p} = 1 \text{ dyn cm}^{-2}$. The number density of H^+ at the lower boundary is set to $n_p = 10^{-4}n_h$. The calculation results are insensitive to the ratio of n_p/n_h . Finally, we assumed $u_\theta = 0$ at the bottom of the atmosphere.

We selected $r_{IMAX} = 7R_p$ as the upper boundary, which approximately denotes the stand-off distance of the planetary wind due to the interaction with the stellar wind. At the upper boundary, we used the outflow boundary conditions. For supersonic outflow, the boundary condition is exact (Stone & Norman 1992). In this paper, we only consider the case of supersonic outflow. The planetary winds can be depressed to subsonic if the stellar winds are strong enough (García Muñoz 2007; Murray-Clay et al. 2009). A full description to the process is beyond the scope of this paper. We will discuss the effect of the interaction with the stellar wind in further work.

We are interested in steady-state solutions. For all hydrodynamic solutions, the steady-state is reached when the relative change in the conservative variables from one time level to the next drops below 10^{-8} . We use a normalized measure defined by (Tóth et al. 1998)

$$\Delta_2 Q = \sqrt{\frac{1}{N_{\text{var}}} \sum_{i=1}^{N_{\text{var}}} \frac{\sum_{\text{grid}} (Q_i^{n+1} - Q_i^n)^2}{\sum_{\text{grid}} (Q_i)^2}}, \quad (20)$$

where N_{var} is the number of conserved variables Q_i , and the superscripts indicate the number of time level.

3. TEST THE ONE-DIMENSIONAL MODEL

To test our model, we started from 1D planetary winds and applied the 1D model to a typical and particular planet sample: HD 209458b. We take the the radius $R_p = 1.4R_J$ and the mass of $M_p = 0.7M_J$, where M_J and R_J are the mass and radius of the Jupiter. The semi-major axis a is set to 0.047AU. The mass of host star is $M_* = 1.148M_\odot$ (<http://exoplanet.eu/>), where M_\odot is the mass of the sun. Note that the tidal acceleration in the 1D model is written as

$$a_r = \frac{GM_*}{(D-r)^2} - G\frac{M_*}{D^3}(D-r), \quad (21)$$

which is same as that of García Muñoz (2007).

Yelle (2004), Tian et al. (2005), García Muñoz (2007) and Penz (2008) have developed time-dependent one-dimensional hydrodynamic models. Thus, a direct comparison with their results can validate the reliability of our model.

With the stellar and planetary physical parameters, the time-dependent results are shown in Figure 2. It is clear from Figure 2 that the time-dependent model predicts the same trends of temperature, velocity and particle number density as do the other models. Those studies that the temperature can attain 8000-10000K at $1.5R_p$ are in agreement with our results. The velocities predicted by our model are higher than those of Yelle (2004), but are similar with those of Tian et al. (2005), García Muñoz (2007) and Penz (2008). The fact that as much as 50% of hydrogen at $r = 2.R_p$ is ionized is a consequence of being irradiated by the host star. Due to lack of photochemistry, the ionization state cannot be predicted accurately by our model. In fact, the atmosphere can be thought of as if made up solely of hydrogen if the amounts of heavy constituents are small enough.

The total mass loss rate of $3.2 \times 10^{10} \text{ g s}^{-1}$ predicted by our model is comparable with the those of Yelle(2004), Tian et al. (2005), Penz (2008) and García Muñoz (2007) (In Table 1, we summarized the cases with $P_{R_p}=10 \text{ dyn cm}^{-2}$ and $P_{10.7} = 200$. The mass loss rate of $2.2 \times 10^{11} \text{ g s}^{-1}$ is comparable with that of García Muñoz (2007)). Some chemical processes are not included in our model. Thus, the net chemical expense of energy cannot be calculated. However, the escape of particles in the atmosphere of planet should be driven mainly by irradiation of host star. Our results show also that the mass loss rates are in good agreement with those of others, thus the effect of chemical energy could be slight.

Yelle(2004) and García Muñoz (2007) have found that the escape rate is energy limited, namely, the escape rate varies roughly with the stellar flux. To test the effect of stellar flux, we multiplied the solar spectrum by factors of 2.2 and recalculated the mass loss rate.

We found that the mass loss rate predicted by the model of 2.2 times solar spectrum is a factor of 3.7 higher than that of solar spectrum. Similar conclusions have also been found by Penz et al. (2008). From Table. 1 in Penz et al. (2008), it is clear that the ratio of mass loss rates are not proportional to the stellar flux. The difference can be explained by a few reasons. First, photochemistry has been neglected in our model and Penz et al. (2008). However, it is unclear whether the photochemistry can affect the ratio of mass loss rates. We will discuss this in future work. Second, we note that the net heating efficiency in our model is defined as $\eta_\nu = (h\nu - 13.6)/h\nu$, which varies with the frequency, but not with radii. In fact, the heating efficiencies should be varied with radii (Yelle 2004). However, the Equation (11) of García Muñoz (2007) expresses that they assumed a net heating efficiency of 100% for all single photons. Our calculations show also that the ratio of mass loss rates decrease to 2.58, roughly equal with the ratio of incident stellar flux, if the net heating efficiency is assumed to 100%. This hints that the heating efficiency plays an important role in simulating the process of the particle escape. Thus, the realistic heating efficiencies of photons in the atmosphere of extra-solar planets should be investigated further by detailed radiative transfer calculations.

An interesting issue is whether a single photon of 20 eV as done in the models of Murray-Clay et al. (2009) and Paper I can denote the stellar EUV irradiation. To test this assumption, we recalculated the model with a single photon of 20 eV (here we assumed that the EUV flux is the same, but we only calculated the radiative transfer of photon of 20 eV) and found that the mass loss rate is $6.1 \times 10^{10} \text{ g s}^{-1}$ which is a factor 2 greater than the value predicted by using whole stellar EUV flux. Moreover, our calculations found that the maximum mass loss rate ($9.55 \times 10^{10} \text{ g s}^{-1}$) is produced when the photon energy is about 26 eV, but photons with higher or lower energy will result in lower mass loss rates. Murray-Clay et al. (2009) predicted a mass loss rate of $3.3 \times 10^{10} \text{ g s}^{-1}$ when incident flux is decreased to $F_{UV}=450 \text{ erg s}^{-1} \text{ cm}^{-2}$ integrated on the the solar flux between photon

energies of 13.6 eV to 40 eV). Applying the similar stellar flux ($F_{UV}=540 \text{ erg s}^{-1} \text{ cm}^{-2}$, the value is half of the whole incident flux), we found that the results calculated by the whole EUV flux can be matched well with a single photon of 22eV. By comparing the ionization, the location of sonic point, temperature structure and mass loss rates, we found that the effect of the whole EUV irradiation can not be substituted by a single photon unless the EUV flux is decreased a factor of 2.

Thus, we can summarize that the effect of the whole EUV irradiation cannot be represented simply by a single photon because different photons penetrate to different depth and supply different heating. The approximation of a single photon erases the characteristics of different photons. In order to obtain reliable results, the contributions from all photons should be included fully.

4. THE TWO-DIMENSIONAL MODELS

4.1. The effect of tidal force

In this section we solved the two-dimensional hydrodynamic equations. To separately discuss the effect of the tidal force, we assumed the case of non-tidal locking, thus the one-dimensional radiative transfer is used (Equation (17)). However, the opacities on the day and night sides may be very different. We will further discuss it in Section 4.2.

The left panels of Figures 3 and 4 show the images of the density (with velocity vectors) and temperature. Note that the density is the sum of hydrogen atoms and ions. In the 2D model, the number density of hydrogen decreases but the ionization fraction increases with radius as does one-dimensional hydrodynamic model. The temperature rises with an increase in radius up to $r/R_p = 2$. The two-dimensional models show that wind temperature can attain 10000K at about $1.5R_p$ and then drop to 3000K.

The mass loss rates are defined as

$$\dot{M} = 2\pi m_{\text{H}}(r_{\text{max}})^2 \left[\int_{\pi}^0 n_h u_r \sin \theta d\theta + \int_{\pi}^0 n_p u_r \sin \theta d\theta \right], \quad (22)$$

where r_{max} is the upper boundary. We obtained a mass loss rate of $\dot{M} = 1.72 \times 10^{10} \text{ g s}^{-1}$ which is a factor of 2 smaller than that calculated by one-dimensional hydrodynamics model.

From Figures 3 and 4, a prominent characteristic is that the contours of the density and temperature are nearly axis-symmetric. It is clear from the left panel of Figure 3 that the pattern of flows are non-radial. The flow vectors show curve toward the equator, and the radial velocities and densities are very low near the polar regions. We have demonstrated this in Figure 5 in which $\frac{n(\theta)}{n(\theta=0)}$ and $\frac{u_r(\theta)}{u_r(\theta=0)}$ at $r=7R_p$ are showed as a function of θ . It is clear that the density and radial velocity decrease rapidly with an increase in θ . The values of $\frac{n(\theta)}{n(\theta=0)} = 0.04$ and $\frac{u_r(\theta)}{u_r(\theta=0)} = 0.2$ at $\theta=90^\circ$ reflect the fact that most particles escape the planet from the zones of low latitude. In fact, the zones of middle-high latitude(45° - 135°) only contribute to 20% of the mass loss rate due to their low density and radial velocity. As a consequence, the mass loss rate of the two-dimensional hydrodynamics is only half of that of one-dimensional hydrodynamics. Figure 6 further shows the effect of tidal forces at different radii. Due to strong gas pressure, the radial velocities are evidently higher than the meridional velocities at the base of the wind ($r/R_p=2$). However, the ratios of u_θ/u_r rapidly increase with an increase in radius. At $r/R_p=4$, the ratio can attain 0.6 at $\theta=70^\circ$, and the value even approaches 1 at $r/R_p=7$. The trend shows how the tidal forces enforce the flows moving in horizontal direction when the gas pressures decrease with an increase in radius. In addition, the peaks of u_θ/u_r are almost emerge at $\theta=70^\circ$ rather than $\theta=90^\circ$ can be attributed to the balance of orbital motions and gravity accelerations of host star.

To further explore the effect of tidal force, we neglected the tidal force and recalculated the model. The right panels of Figures 3 and 4 show spherically symmetric distributions

for density, velocity and temperature. Comparing the left and right panels of Figures 3 and 4, we can find that the tidal forces not only supply strong accelerations in $\hat{\theta}$ direction but also decrease the radial velocity in the polar regions. Therefore, we can draw the conclusion that the tidal forces not only impel the non-radial flows in the planetary atmosphere but also inhibit the escape of particles from the polar regions so that most particles escape the bound of the planet from the zones of low latitude.

4.2. The Case of Tidal Locking

In Section 4.1, we discussed the case of non-tidal locking. However, about 25% extra-solar planets are very close to their host stars thus they should be tidally locked. To inspect the case, we recalculated the two-dimensional planetary winds by using two-dimensional radiative transfer (Equation (18)), which appropriately depicts the irradiation of the host star.

Figure 7 displays that the decline of density on the night sides with the radius is slightly slower than that on day sides. At large radii, the densities of polar regions are lower than that of the regions of low-middle latitude. Close to the planet, the meridional velocities dominant the velocity field and transfer the mass and energy from the day side to the night side (see the left panel of Figure 7 for details). The appearance of strong non-radial flows at the base of the wind can be explained by the variations of the optical depth. The optical depth of single photon of 20 eV for two-dimensional radiative transfer is shown in right panel of Figure 8. The contours of the optical depth extend toward a larger radius from the day side to the night side. When the impact factor q approaches the radius of the planet, the optical depth is in the order of magnitude of $10^{-1} - 10^1$. The heating is proportional to $e^{-\tau}$ (Equation (15)), therefore, more energy can be received on the day side. With an increase in radius, the radial velocities increase gradually. Finally,

the pattern of flows at the base of the wind is nearly in the direction of meridian. In the upper atmosphere, the non-radial flows are comparable with the radial flows, but the radial velocities are stronger in the zones of low-latitude.

The distributions of temperature are also non-spherically symmetric due to the influence of the optical depth (the left panel of Figure 8). Evidently, the distributions of temperature in the night side are controlled by the optical depth. The radiation of the star cannot transmit to those regions where the optical depths are greater than unity. Thus those regions of lower temperature are located at the proximity of impact factor $q \sim 1$ (lower left of right panel of Figure 8). The hottest regions is located at $60^\circ \lesssim \theta \lesssim 180^\circ$ at $r/R_p = 1.3 - 1.8$, which is caused by the balance of PdV work ($P\nabla \cdot \mathbf{v}$), heating, and cooling. To explain the variations of temperature, the contributions of energy at $r/R_p=1.35$ by PdV work, heating, cooling and work W_{ext} done by external forces (gravity of the planet and tidal forces) are shown in Figure 9. Heating from the irradiation and PdV work continuously decline to zero from the day side to night side. However, the work done by external forces continuously rises with the increase of θ . Due to $de = dQ - PdV + W_{ext}$, this hints that external forces can do positive work due to the contraction of gas, which results in the increase of gas temperature (In generally, PdV work expands the atmosphere and lowers the gas temperature.). Therefore, the cause of temperature increase from the day to night side can be explained by the increase of net heating rate. While $105^\circ \lesssim \theta \lesssim 125^\circ$, the temperature slightly declines with the decrease of net heating rate. And eventually, the temperature becomes a constant because the net heating is maintained at a stable level.

We also display the angular slices of the density and velocity at the different radii in Figures 10-12. For comparison, the winds of one-dimensional radiative transfer are also included (solid lines). Seen from Figure 10, the difference in the number density between one- and two-dimensional cases is clear. The total number densities of the two-dimensional

radiative transfer are much less than those of one-dimensional radiative transfer, by a factor of 2-10 (depend on θ). Thus, the mass loss rate also decreases a factor of 4, only $4.3 \times 10^9 \text{ g s}^{-1}$.

The changes of radial velocity with the angles demonstrate different features between the upper and lower atmospheres. In the upper atmosphere ($r/R_p = 4$ and 7), the radial velocities decline with an increase in angle but rise at $\theta = 90^\circ$ again (the left panel of Figure 11). The minimum and maximum radial velocities at $r/R_p = 7$ are 4 ($\theta \approx 90^\circ$) and 21 ($\theta \approx 0^\circ$) km s^{-1} , respectively. In comparing with the case of one-dimensional radiative transfer, the differences decrease with an increase of radius.

However, we also note that the radial velocities at $r/R_p = 2$ almost decline to zero with an increase of θ in the case of two-dimensional radiative transfer. Moreover, the complex behaviors at $r/R_p = 1.5$ reflect the difference between two- with one-dimension radiative transfer (the left panel of Figure 11). This can be attributed to the effect of optical depth. At $r/R_p \approx 1.5$ and 2 , the optical depths can vary few order of magnitude from the day side to the night side, thus the processes of radiative transfer play an important role.

In Figure 12, interesting trends in the angular velocity can be found. First, for both one- and two- dimensional radiative transfers, the meridional velocities show the sine-like profile in the middle-upper atmosphere (the left of Figure 12) and are always negative (positive) if θ is smaller (greater) than $\pi/2$. In contrast, the meridional velocities are always positive at small radii for the case of two-dimensional radiative transfer (the right panel of Figure 12), which reflects the transfer of mass and energy from the day side to the night side. Second, the meridional velocities are comparable with (or even large than) the radial velocities in the middle-high latitude regions of the upper atmosphere. Third, the meridional velocities dominant the velocity field in the base of the wind for the case of two-dimensional radiative transfer, but we have not found similar phenomena in the case of

of one-dimensional radiative transfer.

Therefore, from Figures 7-12, we can conclude that the two-dimensional radiative transfer prominently affects the properties of flow. The influence of velocity field is remarkable at the base of the wind. Due to the large optical depth on the night side, the density decrease a factor of few so that the mass loss rate is a factor of 4 lower than that of one-dimensional radiative transfer. However, the atmosphere becomes transparent with an increase in the radius so that there is moderate difference in the upper atmosphere between the one- and two-dimensional radiative transfer.

5. DISCUSSIONS

We extended our calculations to different cases. The mass loss rates predicted by our models are summarized in Table 1.

5.1. Boundary conditions

So far, our models used $P_{R_p}=1 \text{ dyn cm}^{-2}$ to calculate the mass loss from the surface of the planet. It is unclear what the suitable lower boundary is? Here we have also computed a model in which the lower boundary is set to $P_{R_p}=10 \text{ dyn cm}^{-2}$. As expected, the mass loss rates are higher than those in the cases of $P_{R_p}=1 \text{ dyn cm}^{-2}$. Specially, the mass loss rates enhance 40-70% for the all cases (see Table 1.). This hints that the mass loss rates are very sensitive to lower boundary conditions, and same conclusion has also been found by Penz et al. (2008).

In addition, a possible cause that can lead to the reduction of mass loss rate is the day-night temperature contrasts at the lower boundary. Theoretical studies have shown

that the day-night temperature contrasts (300K or more) are likely to occur in the planetary photospheres (Showman & Guillot 2002). These predictions are also verified by the observed surface temperature distribution of HD 189733b (Knutson et al. 2007).

In the above calculations, we used the same temperature over the lower boundary. In order to further discuss the influence of day-night temperature contrasts, we set the temperature at the lower boundary to

$$T(R_p, \theta) = \begin{cases} 1500K, (\theta \leq 90^\circ) \\ 1500K \max(0.5, \sin \theta), (\theta > 90^\circ). \end{cases} \quad (23)$$

Our results did not show more significant anisotropy for the winds (These results are not presented in this paper.), and the predicted mass loss rates, $4.05 \times 10^9 \text{ g s}^{-1}$, is slightly lower than that of model 9 (see Table 1).

5.2. Dependence of \dot{M} on Stellar Activities

The Swift XRT light curve of HD189733 shows that the escaping hydrogen is observed when the star exhibits a bright flare that occurs about 8 hours before the planetary transit (Lecavelier des Etangs et al. 2012), which implies a possible correlation between the high level of stellar activity and the atmospheric escape of hydrogen. Thus, we also calculated the cases with high level of stellar activity (with a solar proxy $P_{10.7} = 200$). For the high activity, the whole EUV flux is about 2.5 times of the low activity. Our calculations show that the mass loss rates produced by high activity are a factor of 5-10 higher than those of low activity, and the temperatures predicted are also higher. By comparing the structures of wind, we found that the model with higher stellar activity predicted higher radial velocity, and the ratios between meridional and radial velocity are lower. Evidently, higher activities supply more UV radiations, especially in the band of higher energy (note that the increases

of photon energy are not linear with frequency between the low and high stellar activity). More high energy photons mean that the deeper base of the atmosphere can be heated, and the hydrodynamic escape parameter, $\lambda = \frac{GM_p\mu}{R_p kT}$ (μ is mean mass per particle), can decrease to a lower value at deeper atmosphere. Thus gas pressure drives a faster expanding atmosphere and partly counteracts the effect of the optical depth. It explains the reason why the ratio of mass loss rate is only 2.4 for model 8 and 12.

5.3. Comparison with Observations

An interesting issue is which mass loss rate predicted by our model is supported by the observations. Vidal-Madjar et al. (2003) attributed the excess absorption of HD 209458 in Ly α to a mass loss of 10^{10} g s $^{-1}$. Subsequent 1D models also support this. However, the influences of two-dimension and charge exchange between the stellar wind and the planetary escaping exosphere were neglected by all the 1D models. Recently, Lecavelier des Etangs et al. (2012) updated the mass loss rate to 10^9 g s $^{-1}$ for the atmospheric escape of HD 189733b though the previous mass loss rate requested in their model is in the order of magnitude of 10^9 - 10^{11} g s $^{-1}$. Moreover, Holmström et al. (2008) found that a mass loss rate of 7×10^8 g s $^{-1}$ can explain the observations of HD 209458b when the charge exchange is included. We must be careful in the interpretation of mass loss rates because only atomic hydrogen contributes to the excess absorption of Ly α . In our models, the mass loss rates of atomic hydrogen are 3.78×10^8 g s $^{-1}$, 9.85×10^8 g s $^{-1}$, 7.60×10^9 g s $^{-1}$ and 1.45×10^{10} g s $^{-1}$ for models 9-12, respectively. If the charge exchange indeed results in the excess absorption of Ly α , our results favor the low activity for HD 209458 when it is transited by HD 209458b. However, the possibility that planetary origin hydrogen result in excess absorption of Ly α cannot be excluded because Koskinen et al. (2010) explained this by solely absorption in the upper atmosphere based on the 1D assumption. Their

model denotes the averaged property of the atmosphere, but is very different with our 2D hydrodynamic model with consistent radiative transfer. The differences appear in several aspects. First, they estimated a mass loss rate of $1-10 \times 10^{10} \text{ g s}^{-1}$, which is higher than our result. Second, in order to fit the observations, they estimated a number density of $2.6 \times 10^7 \text{ cm}^{-3}$ for hydrogen atoms at $r=2.9R_p$. However, we found that the number densities of hydrogen atoms in our model are about $10^5-10^6 \text{ cm}^{-3}$ at $r=2.9R_p$ (depend on θ), and the number density distributions of hydrogen atoms show clear variations from the day-side to night-side (see Figure. 13). Third, they assumed an ionization of 100% at $r=2.9R_p$. Our results show that the ionization structures of hydrogen strongly depend on θ for the case of tidal-locking. For example, $\frac{n_h}{n_p}=0.16, 0.19$ and 1.08 at $\theta=0, \pi/2$ and π at $r=2.9R_p$. However, our models predicted the similar temperature distributions ($T \approx 7000-11000\text{K}$) below $r=2.9R_p$ as estimated by their models. Thus, one-dimensional models are not accurate enough in calculating the HI transit depth. Our results can be applied further to check if the upper atmosphere contributes significant absorption.

6. CONCLUSIONS

HST observations of HD 209458b and HD 189733b in the UV band have revealed the signatures of atmosphere escape. Theoretical progress is following the observations, for example, reasonable mass loss rates have been predicted by several one-dimensional hydrodynamic models (Yelle 2004; Tian et al. 2005; García Muñoz 2007; Penz 2008; Murray-Clay et al. 2009; Guo 2011). Two-dimensional hydrodynamic model have also revealed a possible anisotropy in the planetary wind (Stone & Proge 2009). However, there exists still a few key problems to be solved, such as the proper descriptions to radiative transfer and charge-exchange reactions between the planetary and stellar wind particles. They play an important role in fully explaining the observations.

Table 1: The mass loss rates for HD 209458b.

Model	$P_{10.7}^a$	$P(R_p)^b$ (dyn cm ⁻²)	Hydrodynamics	Radiative transfer	\dot{M} ($\times 10^{10}$ g s ⁻¹)
1	80	1	1D	1D	3.22
2	80	10	1D	1D	4.78
3	200	1	1D	1D	15.4
4	200	10	1D	1D	20.2
5	80	1	2D	1D	1.72
6	80	10	2D	1D	2.60
7	200	1	2D	1D	12.1
8	200	10	2D	1D	15.6
9	80	1	2D	2D	0.43
10	80	10	2D	2D	0.77
11	200	1	2D	2D	4.50
12	200	10	2D	2D	6.55

^aThe Solar activity proxy.

^bThe pressure at the lower boundary.

In this paper, we presented a two-dimensional multi-fluid hydrodynamic model by incorporating the two-dimensional radiative transfer. From this work, our conclusions are the following.

1. In the assumption of non-tidal locking, the planetary winds are not spherically symmetric. Tidal forces can result in significant horizontal movements in the planetary winds and lower density and radial velocity near the polar regions so that the mass is almost lost fully from the low-latitude zones.

2. In the case of tidal locking, we found that the wind is controlled by meridional velocity in the regions of $r/R_p \sim 1.5$. The large meridional velocities transfer the mass and energy from the day side to the night side at the base of the wind. But the extent decreases with an increase in the radius due to the decrease of the optical depth. At large radii, the wind is significant difference with that of one-dimensional radiative transfer. Due to the declines of density, the mass loss rate is also lower than that of non-tidal locking.

3. The mass loss rates are affected by both two-dimensional radiative transfer and hydrodynamics. Comparing with the results of one-dimensional hydrodynamic models, the models of two-dimensional hydrodynamics predicted the mass loss rates of 1.72 and $0.43 \times 10^{10} \text{ g s}^{-1}$ for one-dimensional and two-dimensional radiative transfer, which are a factor of 2 and 7 smaller than that of 1D hydrodynamic model.

Acknowledgments

The author are grateful to the referee for comments that led to substantive improvements in this work. This work was supported by National Natural Science Foundation of China (Nos.10803018 and 11273054).

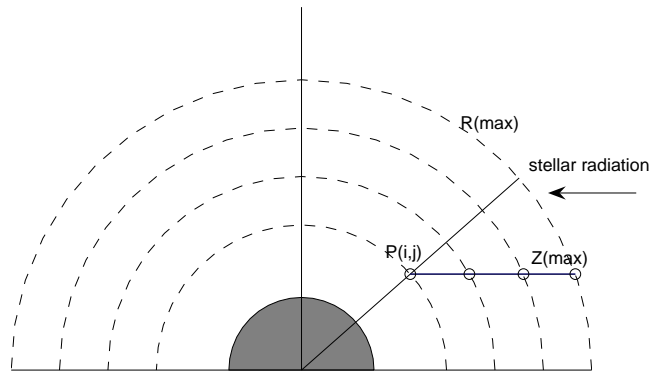


Fig. 1.— Schematic diagram of the calculation method to the optical depth. The circles represent the nodal points at other radii. i represents the radial grid. j denotes the angular grid.

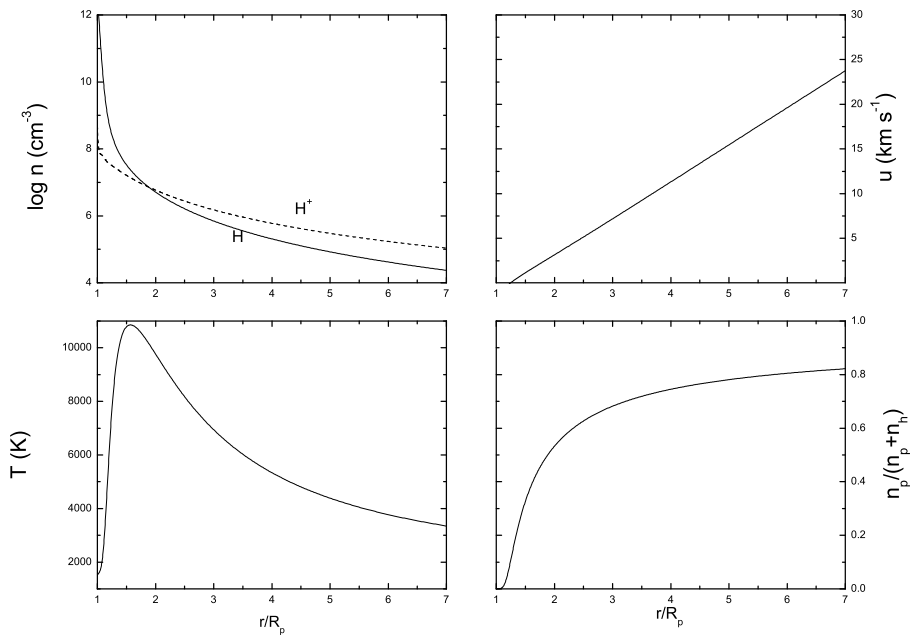


Fig. 2.— The one-dimensional wind model for HD 209458b. Number densities (upper left), velocities (upper right), temperatures (lower left) and the ionization fraction (lower right) are plotted as the functions of altitude.

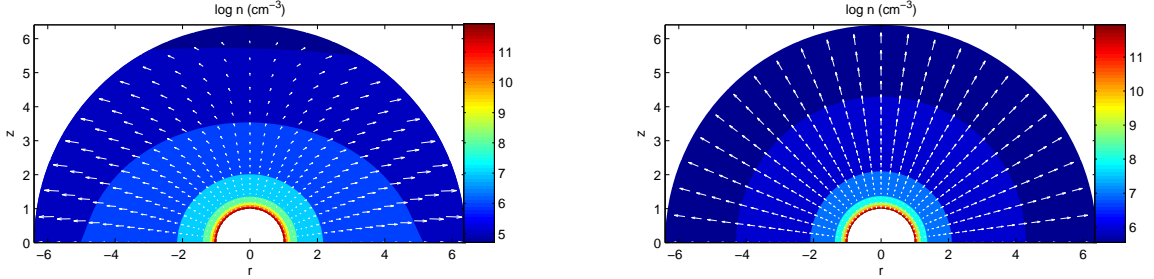


Fig. 3.— The results of two-dimensional hydrodynamic model with one-dimensional radiative transfer. Left: density and velocity vectors for the case with tidal forces. Right: density and velocity vectors for the case without tidal forces. The host star is located toward the right (corresponding to $\theta = 0$).

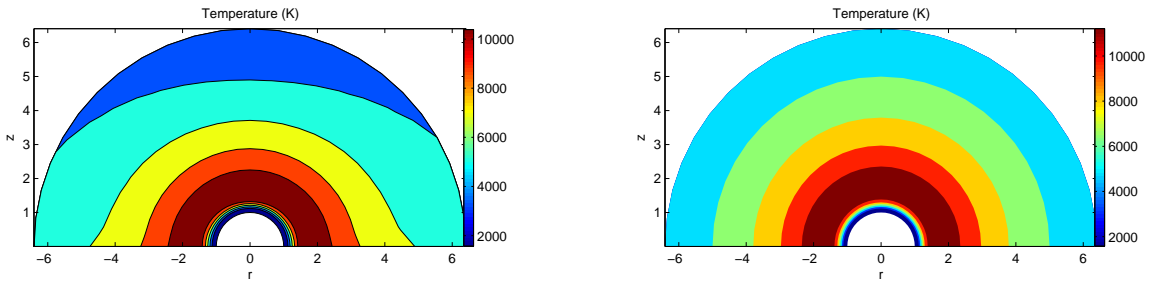


Fig. 4.— The results of two-dimensional hydrodynamic model with one-dimensional radiative transfer. Left: temperature distributions for the case with tidal forces. Right: temperature distributions for the case without tidal forces. The host star is located toward the right (corresponding to $\theta = 0$).

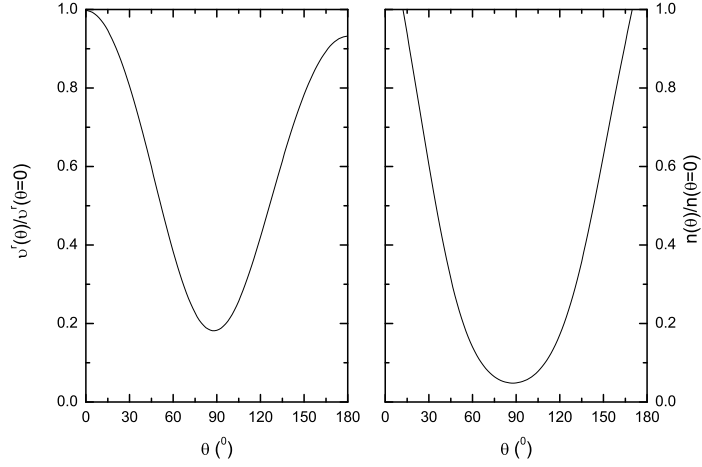


Fig. 5.— Left: the radial velocity v^r as a function of θ at $r/R_p=7$. Right: the distributions of number density as a function of θ at $r/R_p=7$.

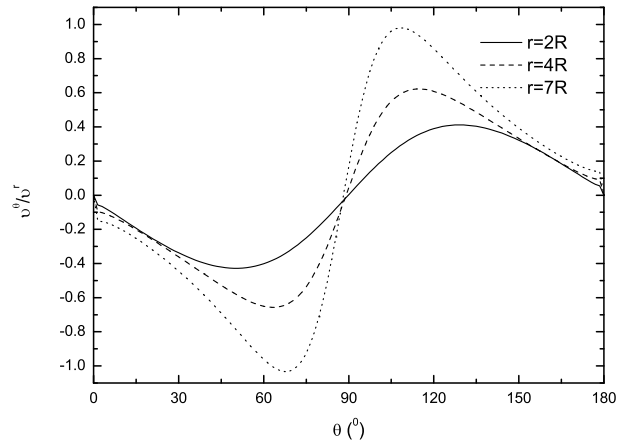


Fig. 6.— The values of u_θ/u_r as a function of θ at $r/R_p=2, 4$ and 7 .

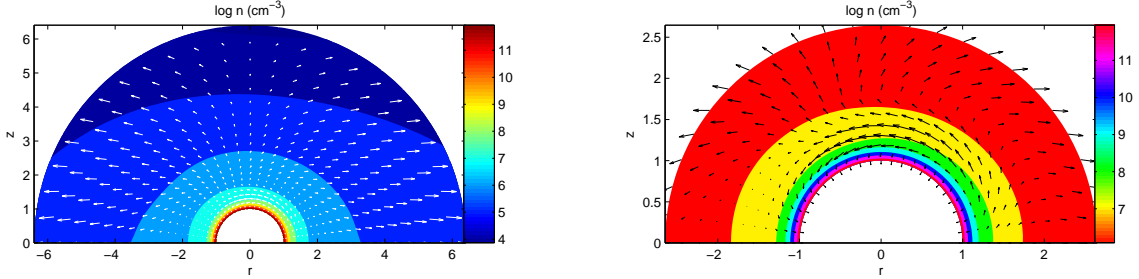


Fig. 7.— The results of the two-dimensional hydrodynamic model with two-dimensional radiative transfer. Left: density and velocity vectors at $1 \leq r/R_p \leq 7$. Right: density and velocity vectors at the atmospheric base ($1 \leq r/R_p \leq 2.6$).

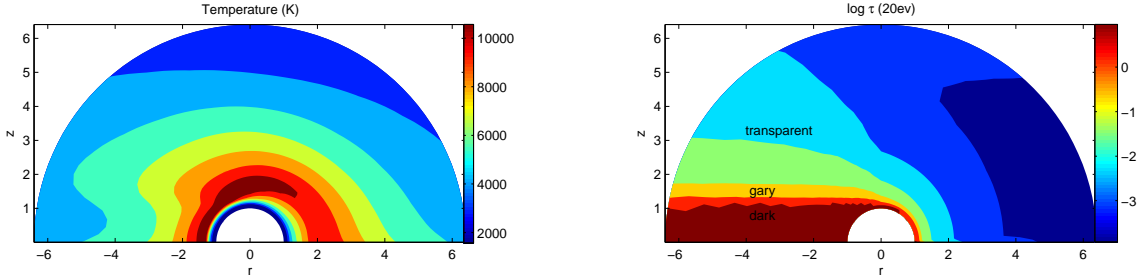


Fig. 8.— The results of the two-dimensional hydrodynamic model with two-dimensional radiative transfer. Left: the distributions of temperature. Right: the distributions of the optical depth. In the right panel the optical depth larger than 10 is marked with "dark". The "gray" region denotes the case of $10^{-1} < \tau < 1$. In the transparent region, the optical depth is smaller than 10^{-1} .

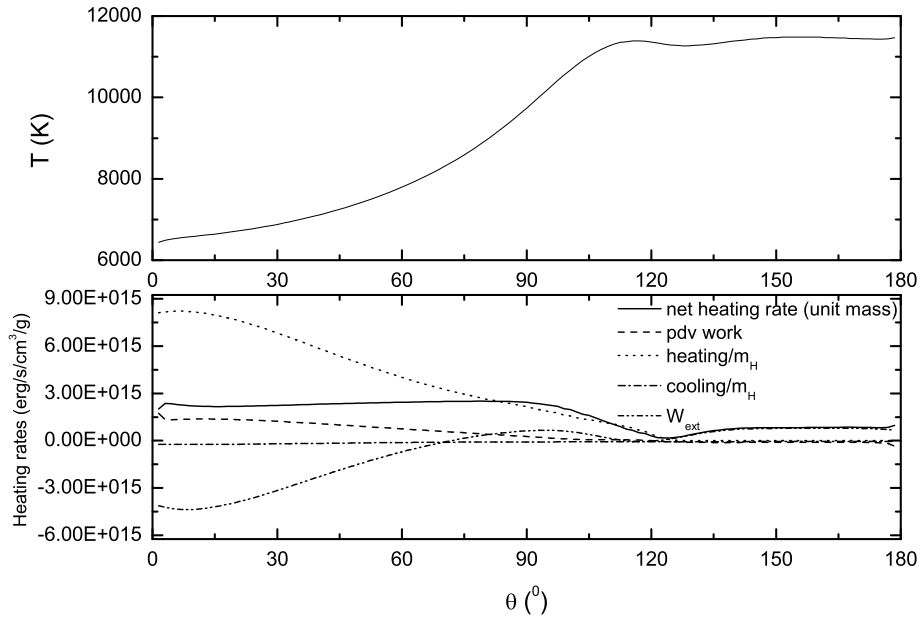


Fig. 9.— Temperatures and heating rates (unit mass) in the model. In the lower panel, the solid line represents the net heating rate in the atmosphere. The dashed, dotted and dash-dotted lines denote the PdV work, heating from host star and cooling. The term W_{ext} (dash-dot-dotted) represents the work made by the gravity of planet and tidal forces.

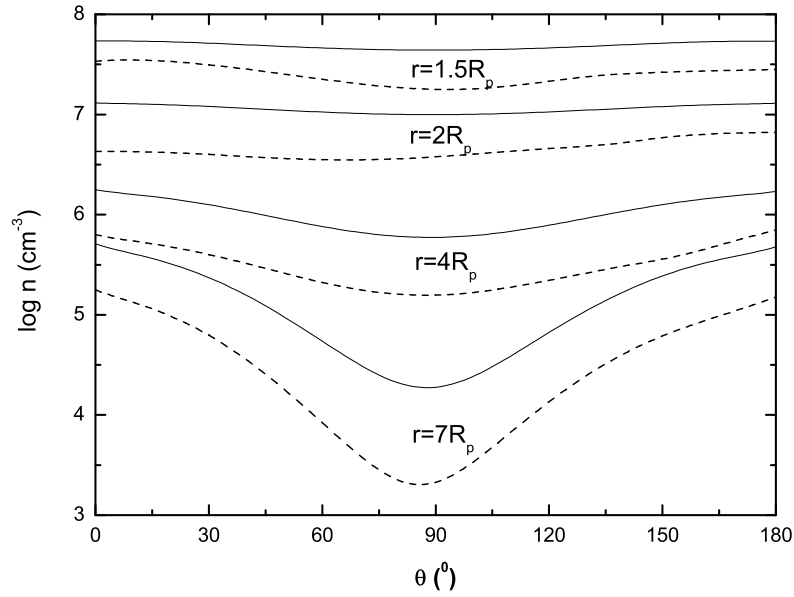


Fig. 10.— Number densities at $r/R_p = 1.5, 2, 4$ and 7 (from top to bottom). Solid lines represent the case of one-dimensional radiative transfer. Dashed lines represent the case of two-dimensional radiative transfer. Note: The number densities are the sum of hydrogen atoms and ions.

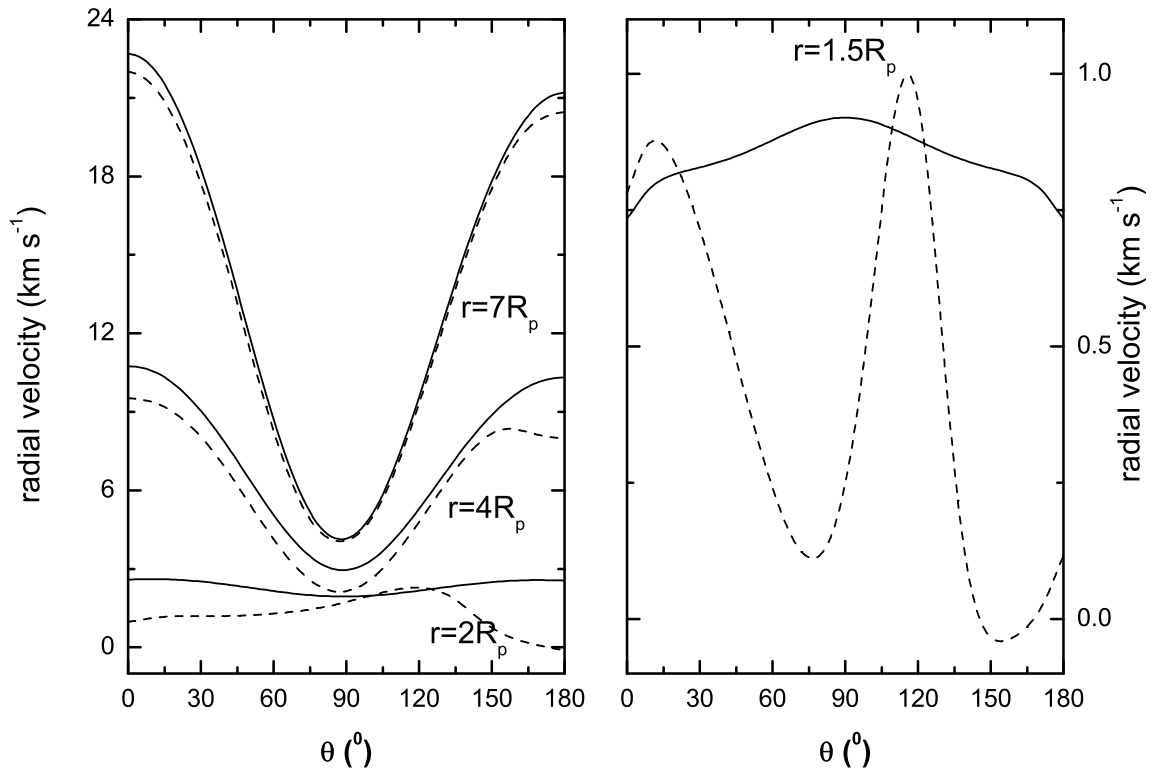


Fig. 11.— Left: radial velocities at $r/R_p = 2, 4$ and 7 . Right: radial velocities at $r/R_p = 1.5$. Solid lines represent the case of one-dimensional radiative transfer. Dashed lines represent the case of two-dimensional radiative transfer.

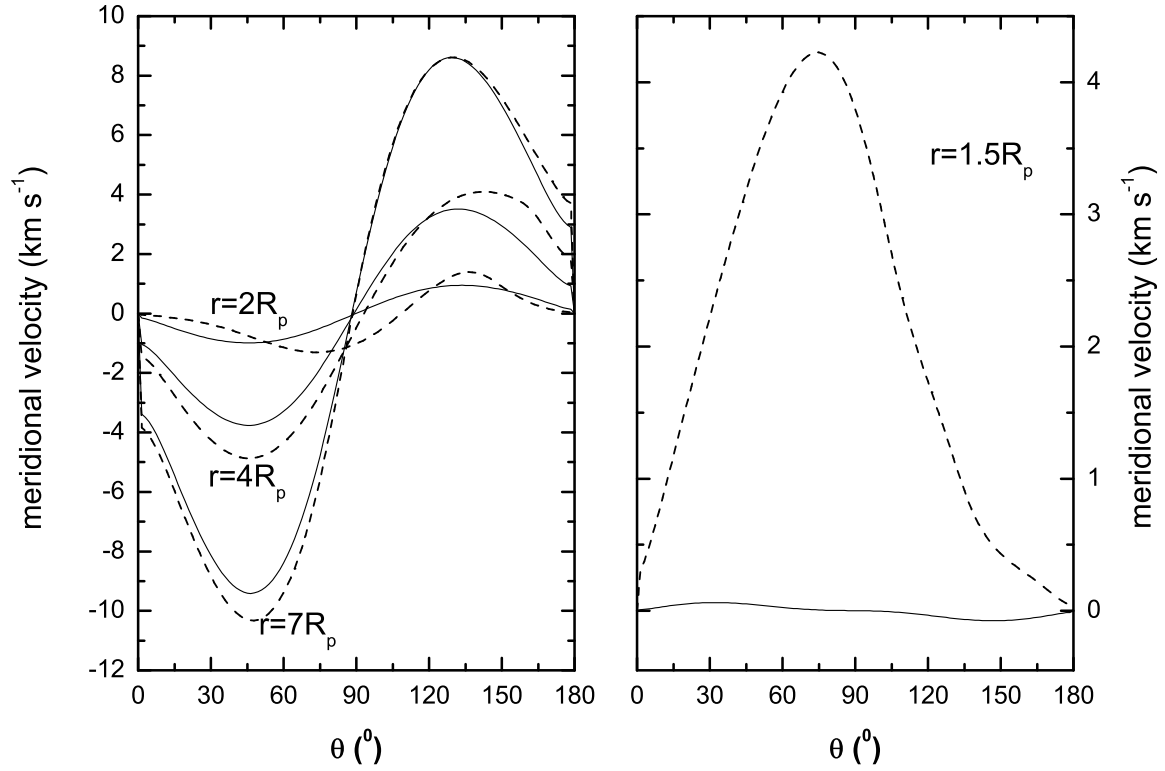


Fig. 12.— Left: meridional velocities at $r/R_p = 2, 4$ and 7 . Right: meridional velocities at $r/R_p = 1.5$. Solid lines represent the case of one-dimensional radiative transfer. Dashed lines represent the case of two-dimensional radiative transfer.

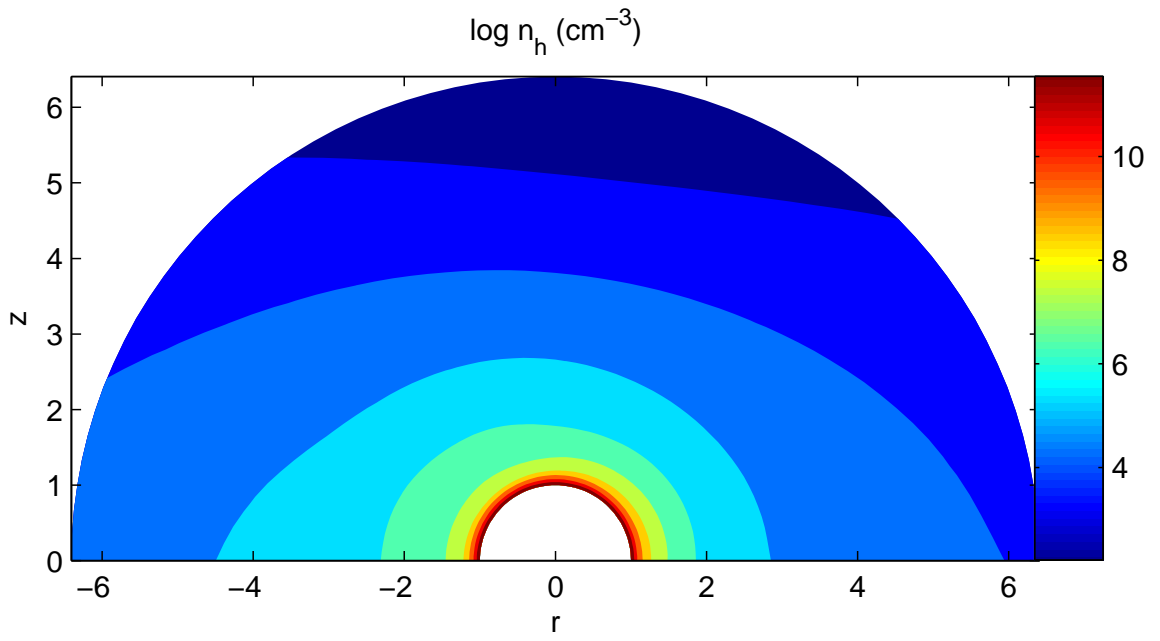


Fig. 13.— The number density distributions of hydrogen atoms in the case of the two-dimensional hydrodynamic model with two-dimensional radiative transfer.

REFERENCES

- Ben-Jaffel, L., & Hosseini, S. S. 2010, *ApJ*, 709, 1284
- Burrows, A., Hubbard, W. B., Lunine, J. I., & Liebert, J. 2001, *Rev. Mod. Phys.* 73, 719
- Charbonneau, D., Allen, L. E., Megeath, S. T., Torres, G., Alonso, R., Brown, T., Gilliland, R. L., Latham, D. W., Mandushev, G., O'Donovan, F. T., & Sozzetti, A. 2005, *ApJ*, 626, 523
- Deming, D., Seager, S., Richardson, L.J., & Harrington, J. 2005, *Nature*, 434,740
- Deming, D., Harrington, J., Seager, S., & Richardson, L.J. 2006, *ApJ*, 644, 560
- Erkaev, N. V., Penz, T., Lammer, H., Lichtenegger, H. I. M., Biernat, H. K., Wucz, P., Grieß Meier, J. M., & Weiss, W. W. 2005, *ApJs*, 157, 396
- Ekenbäck, A., Holmström, M., Wucz, p., Griessmeier, J. M., Lammer, H., Selsis, F., & Penz, T. 2010, *ApJ*, 709, 670
- Garcia Munoz, A. 2007, *Planet. Space Sci.*, 55, 1426
- Guillot, T., Burrows, A., Hubbard, W. B., Lunine, J. I., & Saumon, D. 1996, *ApJ*, 459, L35
- Guo, J. H. 2011, *ApJ*, 733, 98 (Paper I)
- Holmström, M., Ekenbäck, A., & Selsis, F., et al. 2008, *Nature*, 451, 970
- Knutson, H. A., Charbonneau, D., & Allen, L. E., et al. 2007, *Nature*, 447, 183
- Koskinen, T. T., Yelle, R. V., Lavvas, P. L., & lewis, N. K. 2010, *ApJ*, 723, 116
- Lammer, H., Selsis, F., Ribas, I., Guinan, E. F., Bauer, S. J., & Weiss, W. W. 2003, *ApJ*, 598, L121

- Lammer, H., Odert, P., Leitzinger, M., & Weiss, W. W., et al. 2009, *A&A*, 506, 399
- Lammer, H., Odert, P., Leitzinger, M., & Weiss, W. W., et al. 2011, *Ap&SS* tem, 278
- Lecavelier des Etangs, A., Vidal-Madjar, A., McConnell, J. C., & Hbrard, G. 2004, *A&A*, 418, L1
- Lecavelier Des Etangs, A., Ehrenreich, D., Vidal-Madjar, A., Ballester, G. E., Dsert, J.-M., Ferlet, R., Hbrard, G., Sing, D. K., Tchakoumegni, K.-O., & Udry, S. 2010, *A&A*, 514, 72
- Lecavelier des Etangs, A., Bourrier, V., Wheatley, P. J., Dupuy, H., Ehrenreich, D., Vidal-Madjar, A., Hébrard, G., Ballester, G. E., Désert, J. M., Ferlet, R., & Sing, D. K. 2012, arXiv. 1206.6274
- Murray-Clay, R. A., Chiang, E. I., & Murray, N. 2009, *ApJ*, 693, 23
- Penz, T., Erkaev, N. V., & Kulikov, Y. N., et al. 2008, *Planet. Space Sci.*, 56, 1260
- Richards, P. G., Fennelly, J. A., & Torr, D. G. 1994, *JGR*, 99, 8981
- Schneider, E. M., Velázquez, P. F., Esquivel, A., & Raga, A. C. 2007, *ApJ*, 671, L57
- Showman, A. P., & Guillot, T. 2002, *A&A*, 385, 166
- Stone, J. M., & Norman, M. L. 1992, *ApJ*, 80, 753
- Stone, J. M., & Proga, D. 2009, *ApJ*, 694, 205
- Tian, F., Toon, O. B., Pavlov, A. A., & De Sterck, H. 2005, *ApJ*, 621, 1049
- Tóth, G., Keppens, R., & Botchev, M. A. 1998, *A&A*, 332, 1159
- Trilling, D. E. 2000, *ApJ*, 537, L61

Vidal-Madjar, A., Lecavelier des Etangs, A., Dsert, J.-M., Ballester, G. E., Ferlet, R.,
Hbrard, G., & Mayor, M. 2003, *Nature*, 422, 143

Yelle, R. 2004, *Icarus*, 170, 167

Yelle, R. 2006, *Icarus*, 183, 508